metals

MDPI

Article

Laser Powder Bed Fusion Processing of Fe-Mn-Al-Ni Shape Memory Alloy—On the Effect of Elevated Platform Temperatures

Felix Clemens Ewald [1], Florian Brenne [1], Tobias Gustmann [2], Malte Vollmer [1], Philipp Krooß [1,*] and Thomas Niendorf [1]

[1] Institute of Materials Engineering—Metallic Alloys, University of Kassel, 34125 Kassel, Germany; Ewald@uni-kassel.de (F.C.E.); florian.brenne@gmail.com (F.B.); vollmer@uni-kassel.de (M.V.); niendorf@uni-kassel.de (T.N.)

[2] Leibniz IFW Dresden, Institute for Complex Materials, 01069 Dresden, Germany; t.gustmann@ifw-dresden.de

* Correspondence: krooss@uni-kassel.de

Abstract: In order to overcome constraints related to crack formation during additive processing (laser powder bed fusion, L-BPF) of Fe-Mn-Al-Ni, the potential of high-temperature L-PBF processing was investigated in the present study. The effect of the process parameters on crack formation, grain structure, and phase distribution in the as-built condition, as well as in the course of cyclic heat treatment was examined by microstructural analysis. Optimized processing parameters were applied to fabricate cylindrical samples featuring a crack-free and columnar grained microstructure. In the course of cyclic heat treatment, abnormal grain growth (AGG) sets in, eventually promoting the evolution of a bamboo like microstructure. Testing under tensile load revealed a well-defined stress plateau and reversible strains of up to 4%.

Keywords: additive manufacturing; laser powder bed fusion; shape memory alloy; Fe-Mn-Al-Ni; cyclic heat treatment

Citation: Ewald, F.C.; Brenne, F.; Gustmann, T.; Vollmer, M.; Krooß, P.; Niendorf, T. Laser Powder Bed Fusion Processing of Fe-Mn-Al-Ni Shape Memory Alloy—On the Effect of Elevated Platform Temperatures. *Metals* **2021**, *11*, 185. https://doi.org/10.3390/met11020185

Academic Editor: Gabriel A. Lopez

Received: 27 December 2020

Accepted: 15 January 2021

Published: 20 January 2021

1. Introduction

During the past decades, the development of new shape memory alloys (SMAs) gained a lot of interest in academia and the industry, in order to meet the demand for light and extremely compact actuators and damping devices. It is well-known that binary Ni-Ti SMAs suffer from poor cold workability, relatively high costs, as well as a narrow temperature window for practical application, limiting a more widespread industrial usage [1]. Thus, other SMA systems came into focus of academic and industrial research to extend the application range, e.g., to higher transformation temperatures, as in the case of Ni-Ti-Hf alloys [2], or to higher application frequencies, as in the case of magnetic SMAs [3,4]. For providing more economic, low-cost SMAs, substantial work was conducted on iron-based SMAs, such as Fe-Mn-Si [5], Fe-Ni-Co-Al-Ta [6], and Fe-Mn-Al-Ni [7]. Based on these alloys it is possible to realize novel applications, e.g., in the construction sector [8].

However, good functional properties strongly require adequate microstructures in Fe-based SMAs. Thus, the microstructure should be tailored with respect to the crystallographic orientation, grain size, grain morphology, and phase fractions, in order to enable high transformation strains, good reversibility, as well as cyclic stability [5,9–17]. Thus, complex thermo-mechanical treatments like combined hot-cold rolling, wire drawing, and cyclic heat treatments were investigated in several studies [5,9–17]. However, even if there is reasonable progress, efforts spent on thermomechanical processing are tremendous, and up to now microstructure design in Fe-based SMAs still remains challenging.

With the emergence of the additive manufacturing (AM) technologies, such as laser powder bed fusion (L-PBF) or electron beam powder bed fusion (E-PBF), which enable the

production of components, layer by layer, on the basis of a computer-aided design (CAD) file, new possibilities are opened up. Based on this principle, a high geometric complexity is offered without the need of tooling operations [18]. Furthermore, via L-PBF and E-PBF, the microstructure with respect to grain size, grain morphology, and texture can be tailored by applying different exposure strategies for melting the initial powdery starting material, e.g., as shown for Ni-base alloys [19], aluminum [20], and stainless steel 316 L [21,22]. In consequence, processing of SMAs by AM techniques came into focus of research [23–26]. Numerous studies focused on AM of Ni-Ti revealed that the processing window of Ni-Ti seems to be rather small [27]. Recently, some of the current authors investigated AM of Fe-Mn-Al-Ni by L-PBF [28] as well as E-PBF [29]. It was shown that the alloy is generally suitable for processing by both AM techniques. Adequate functional properties were revealed after additional heat treatments. These post treatments aimed at promoting abnormal grain growth (AGG) [16,30] and precipitate formation [31]. However, up to now, superelastic properties were only shown under compressive loading. Most detrimentally, crack formation occurred especially in material processed by L-PBF. Since it is well known that rapid quenching and cooling, respectively, can lead to crack formation in Fe-Mn-Al-Ni [17], it is likely that cracking occurs due to the high cooling rates and the general thermal history prevailing in L-PBF during processing. To substantiate this assumption, in the present study, Fe-Mn-Al-Ni was processed using a built platform heated up to 500 °C during processing, in order to ensure lower cooling rates during processing and, eventually, promote crack-free conditions, showing superelastic properties in tension.

2. Materials and Methods

Commercially pure Fe-Mn-Al-Ni, produced by vacuum induction melting, with a nominal chemical composition of Fe-34-Mn-14-Al-7.5-Ni (at.%), i.e., Fe 48.1-Mn 36.1. Al 7.3 Ni 8.5 (wt.%), was cast by Stahlzentrum Freiberg e.V. (Freiberg, Germany). Subsequently, the material was gas atomized under argon atmosphere by TLS Technik GmbH (Bitterfeld, Germany). The resulting mean particle size (d_{50}) of the powder used for laser powder bed fusion was 40 µm. Using a SLM250^{HL} machine (SLM Solutions Group AG, Lübeck, Germany), cubes of 5 mm × 5 mm × 7 mm, cylinders of 5 mm in diameter, and 40 mm in height, as well as pillars/rods with diameters ranging from 0.5 to 3 mm (height: 7 mm) were fabricated. From the cylinders, the tensile samples were fabricated by electrode discharge machining. The pillars were conventionally separated from the baseplate and used for the evaluation of the geometric/dimensional impact on microstructure evolution. The build platform (in-house development of Leibniz IFW [32], see Figure 1 for details) was heated to 500 °C before processing. A laser power of 200 W, scan speed of 680 mm s^{-1}, hatch distance of 0.12 mm, and a layer thickness of 30 µm, were employed for sample processing (stripe scanning, −90° scan vector rotation). After the build job ended, the baseplate temperature was further held constant for 15 min followed by slow cooling to 400 °C and switching of the heating system. After the aforementioned cooling phase, the sample setup was quickly removed and placed on an iron-cast block to allow faster cooling to room temperature.

Beside the as-built state, selected samples were heat-treated in evacuated quartz tubes. In a first step, a solution heat treatment at 1200 °C for 12 h was followed by water quenching. Afterwards, defined heat treatment cycles (HTC) were applied. Details on the procedure are depicted in Section 3 for clarity. In the present work, three and five HTC were applied to the selected samples, followed by quenching in 80 °C tempered water.

The chemical composition of the powder and the bulk material (L-PBF samples) was analyzed using ICP-OES (Inductively-Coupled Plasma–Optical Emission Spectroscopy, IRIS Intrepid II XUV from Thermo Fischer Scientific, Waltham, MA, USA). Furthermore, the oxygen (LECO TC-436DR—powder and L-PBF) and hydrogen content (HORIBA EMGA 621 W—powder only) were determined in order to exclude contamination of the powder and the L-PBF processed bulk. A minimum of three measurements were performed to obtain the experimental average values and corresponding deviations.

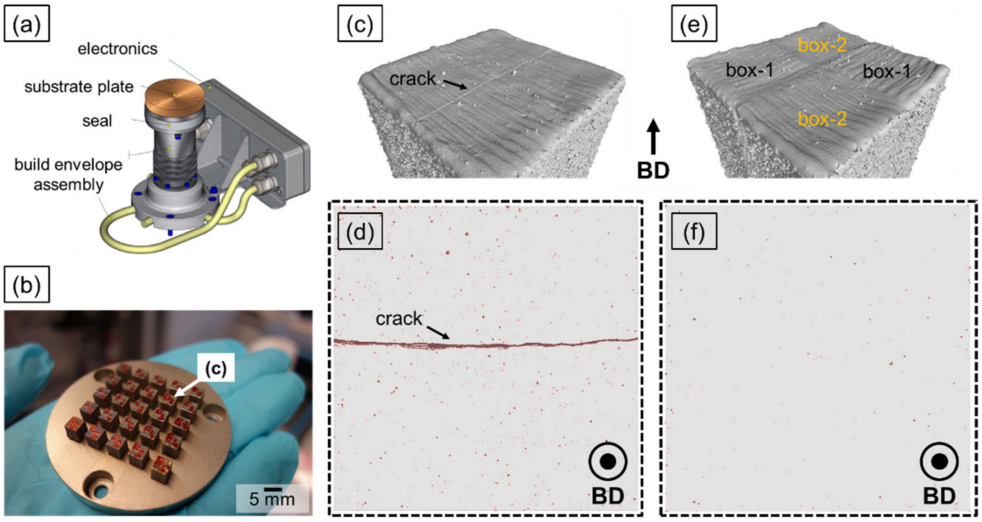

Figure 1. Overview of the machine setup used and selected Fe-Mn-Al-Ni samples fabricated at Leibniz IFW Dresden. An in-house developed build envelope (substrate plate diameter of 67 mm) was used for processing at a fixed temperature of 500 °C (**a**). Process parameter optimization for Fe-Mn-Al-Ni (**b**) considering varying laser power (right to left: 125–225 W) and scanning speed (top to bottom: 610–890 mm/s). Reconstructed CT-images (**c**–**f**) revealing that crack free samples (5 mm × 5 mm × 7 mm) can be manufactured using the optimized parameters laser power = 200 W, scanning speed = 680 mm/s, hatching distance = 0.12 mm, in combination with (**e**,**f**) a chessboard-like scanning pattern (2.5 mm × 2.5 mm × 2 mm box size). Box-1 and box-2, as depicted in (**e**) were scanned perpendicular to each other and were constantly rotated layer-by-layer, by 90°. Numerous pores and a major crack in case of (**c**,**d**) conventional stripe scanning without island separation are shown in red. Please note that the images in (**d**,**f**) show the analyzed, transparent volume of the cubes (top view) shown in (**c**,**e**), respectively.

In order to see if the samples could be processed crack-free and with a low residual porosity, selected samples, fabricated with the optimized process parameters and the high-temperature build envelope, were investigated using a Phoenix Nanotom M (General Electric) computer tomograph (referred to as CT). The resolution of the CT was set to 6 µm, using an acceleration voltage of 135 kV and a current of 100 µA. CT-scans were performed using a beam collimator and copper filter (0.3 mm in thickness). 700 projections were recorded in total for the reconstruction of a single 3D-model. Volume analysis was carried out using VG-Studio max 2.2 (Volume Graphics). Artefacts and imperfections (voids with low sharpness) below the voxel size were digitally filtered out and not further considered.

For scanning electron microscopy (SEM), the samples were mechanically ground, polished down to 5 microns, and finally vibration polished. The SEM used was operated at 20 kV and equipped with an electron backscatter diffraction (EBSD) unit (EDAX Inc, Mahwah, NJ, USA). From EBSD data inverse pole figure (IPF) maps were obtained using standard software tools (EDAX OIM software, version 7, EDAX Inc, Mahwah, NJ, USA). The Vicker's hardness was probed using a load of 4.9 N (HV 0.5). Mechanical testing (controlled loading/unloading cycles) was conducted using flat small dog-bone shaped samples with a gage section of 18 mm, with 1.5mm x 1.5 mm cross section, electro-discharge machined from the as-built cylinders (diameter = 5 mm, height = 40 mm). A servohydraulic testing rig was used at a crosshead displacement speed of 0.01 mm s^{-1}. An extensometer was directly attached to the sample gage section.

3. Results and Discussion

L-BPF processing of the Fe-34Mn-14Al-7.5Ni shape memory alloy at a build platform temperature of 500 °C resulted in a crack-free microstructure in the as-built condition. In Fe-Mn-Al-Ni, several precipitation processes take place as a function of time and temperature [33,34]. From room temperature (RT) up to about 400 °C, small nanometric

β-phase precipitates form upon aging, within minutes or hours, depending on the aging temperature applied. Niendorf et al. [28] reported that due to the formation of the β-type precipitates and due to the high cooling rates induced by a relatively low build platform temperature of up to 200 °C, significant crack formation occurs following L-PBF processing. It was stated that L-PBF processing at 200 °C leads to a strong increase of the hardness, resulting in an embrittlement of the microstructure. Eventually, the high cooling rates during L-PBF processing and the evolution of internal stress fields led to significant crack formation [28]. In the present study, the platform temperature was fixed at 500 °C. Obviously, this had a significant impact on the thermal history and, thus, on the sample quality and the microstructural evolution. While the thermal gradient during processing is significantly higher in case of a build platform temperature of only 200 °C, a build platform temperature of 500 °C promotes lower cooling rates, as well as a less pronounced defect formation (cracks, pores, etc.) during processing (Figure 1c–f).

The as-built microstructure was processed and probed in the form of small cylinders of different diameters, in order to evaluate the impact of geometry/dimensions on microstructural evolution (Figure 2). In the as-built condition, the increase in sample diameter from 0.5 mm to 3 mm (Figure 2a–d) led to a coarser grained microstructure and a significantly stronger texture along the [001] direction parallel to the build direction (BD). The formation of strong textures and columnar grained microstructures is strongly promoted by the highest thermal gradient (G) and the solidification velocity (V) during processing, as reported in numerous studies [21,22,26]. Thus, adjusting the process parameters allows for a microstructural design of metallic alloys, at least for a constant geometry and constant sample dimensions. However, in the case of fixed processing parameters, geometry affects G and V, at least when very small dimensions of cross-sections are considered.

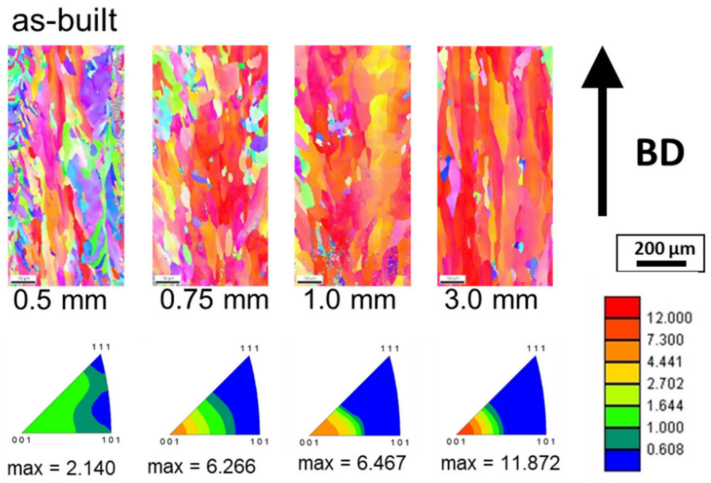

Figure 2. Electron backscatter diffraction (EBSD) inverse pole figure (IPF) maps of additively manufactured Fe-Mn-Al-Ni samples plotted in build direction (BD) for diameters ranging from 0.5 mm to 3 mm for the as-built condition (**a–d**). BD indicates the build direction. The color-coded triangles reveal the maximum texture. The relevant legend coding texture intensity is shown on the right side (max. 12.000).

From the results shown in Figure 2, it can be directly deduced that the variation in geometrical dimensions of the as-built parts is linked to a change in the evolution of the microstructure. As stated before, this is related to a change in G and V, both values being simultaneously affected by the volume energy, scanning strategy, and the build platform temperature. In an earlier study by some of the current authors, a build platform temperature of 200 °C was used during L-PBF processing, leading to a similar kind of microstructure transition, as compared to the current work [28]. However, in that study the strongest texture was observed in the smaller diameter cylinders and not, as shown in the present results, in samples featuring relatively large diameters. Since most L-PBF

process parameters (laser power, scan velocity, etc.) were generally similar in both studies, the build platform temperature is supposed to have the most significant impact on the evolution of the microstructure at this point. It can be deduced that the higher build platform temperature led to a change in the overall thermal history during processing, directly affecting the solidification character, and eventually, the final grain morphology and orientation.

The applied heat treatment procedure employed to stimulate AGG is depicted in Figure 3a. Figure 3b–d shows the impact of the repetition of the HTC for 1, 3, and 5 times, for the given heat treatment procedure (Figure 3a). In Figure 3b, after 1 HTC, a columnar, fine-grained microstructure is seen. Already after 3 HTC (Figure 3c), a change towards a coarser grained microstructure is obvious. A large grain formed by consuming the initially columnar grains. After 5 HTC significant grain growth occurred, and a single grain of around 7 mm characterized by the <111> direction could be identified (Figure 3d). Thus, from the IPF maps presented, it was obvious that the AGG occurred in the additively manufactured Fe-Mn-Al-Ni. However, the results indicated certain inhomogeneities in the microstructure, i.e., the initial texture was not strong enough to be transferred into the abnormally grown grains.

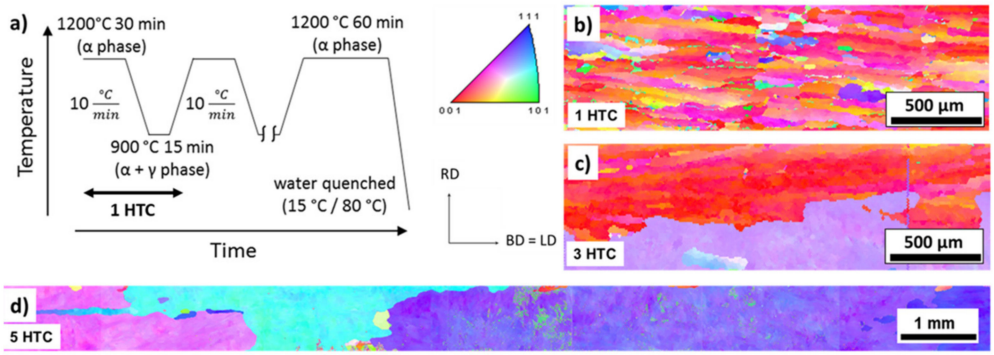

Figure 3. (**a**) Schematic highlighting a single heat treatment cycle (HTC) step (horizontal arrow) of the procedure employed to promote abnormal grain growth (AGG). (**b**–**d**) EBSD IPF maps depicting the cyclically heat-treated samples plotted in BD, after 1 HTC (**b**), 3 HTC (**c**), and 5 HTC (**d**).

Vickers hardness tests on all samples in the as-built condition, as well as after 1 and 5 HTC (without aging) were conducted (Figure 4). The as-built condition showed a noticeably higher hardness than those samples following 1 or 5 HTC. A similar result was observed in the already mentioned former study, where the hardness in the as-built condition increased up to 420 HV [28]. L-PBF processing at a build platform temperature of 200 °C resulted in the formation of nanoscaled β-phase precipitates in the L-PBF-processed Fe-Mn-Al-Ni alloy and, in consequence, led to a significant increase in hardness, as compared to a solution-treated condition. As detailed before, it was reported in several other studies (primarily focusing on conventionally processed material) that an artificial aging at 200 °C led to the formation of the β-phase precipitates, and thus, material strength and hardness can be substantially increased. In the present study, the elevated platform temperature of 500 °C obviously also had a significant impact on the hardness, since in the as-built condition, the hardness was even found to be higher than in the former study [28], i.e., 600 HV in present work (Figure 4). This difference clearly indicates that precipitates might also have formed during L-PBF processing at 500 °C. Moreover, it is likely that β-Mn phase evolved here. It was already reported for conventionally processed Fe-Mn-Al-Ni that above 300 °C, the β-Mn phase evolves in addition to the β-phase precipitates [33,34]. Taking into account that following L-PBF processing the samples were held at 400 °C for 15 min, it could be assumed that the high hardness values following L-PBF processing at 500 °C, were at least partly related to the formation of the β-Mn phase. However, the related increase in hardness did not seem to affect the formation of defects upon

quenching, since no significant defect formation was observed in the material following processing at 500 °C (Figure 1). In other words, the build platform temperature seemed to be high enough to impede any kind of process-related cracking mechanism during processing and subsequent cooling.

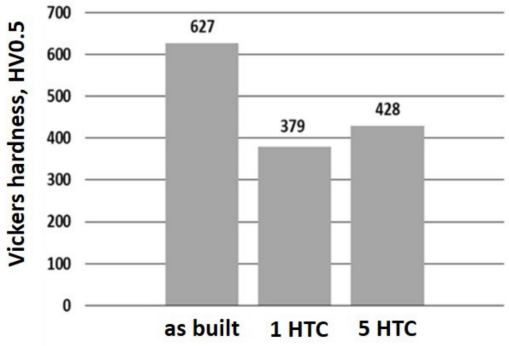

Figure 4. Vickers hardness of laser powder bed fusion (L-PBF) processed Fe-Mn-Al-Ni in the as-built condition, as well as after 1 and 5 HTCs.

In the course of any heat treatment routes considered, the as-built condition was solutionized and both the nano scaled β-precipitated and the β-Mn phase dissolved, eventually leading to a decrease in hardness to about 379 HV and 428 HV for 1 HTC and 5 HTC, respectively. This was in line with the findings presented in previous work [28]. Considering the grain growth induced by the HTC (Figures 2 and 3), the slight increase of hardness after 5 HTC (Figure 4) could be linked to the abnormally grown grains, i.e., the local effect of crystallographic grain orientation of abnormally grown grains, or marginal differences in quenching rates, eventually affecting the absolute value of Vickers hardness.

Analysis of the chemical composition of different conditions revealed a significant loss in the Mn content (Table 1) in the L-PBF processed condition. Whereas the nominal chemical composition contains 34 at. % of manganese, high-temperature L-PBF processing obviously results in a loss of around 3 at. % of Mn. Thus, a considerable change in the functional material properties, e.g., critical stresses for phase transformation, transformation temperatures, and phase stabilities, had to be expected. However, although this change in chemical composition is significant, the superelastic properties of the studied Fe-Mn-Al-Ni alloy are seen to be very promising (Figure 5).

Table 1. Nominal and experimentally determined chemical compositions of Fe-Mn-Al-Ni characterized in form of powder and L-PBF processed bulk material. The relative standard deviation (three measurements) was found to be below 1%.

Chemical Composition	Nominal	Powder	As Built
Ni (at. %)	7.50	7.49	7.87
Al (at. %)	15.00	15.44	15.88
Mn (at. %)	34.00	33.21	30.81
Fe (at. %)	43.50	42.52	44.86

Figure 5a depicts the stress–strain response obtained at RT under tensile loading for a Fe-Mn-Al-Ni sample initially processed by L-PBF. Such data are shown for the first time in literature. Following 5 HTC, good superelastic material properties can be seen (Figure 5), being similar to other stress–strain hysteresis curves shown in literature [35]. The critical stress for stress induced phase transformation (SIMT) was about 405 MPa. Following the first loading cycle up to 2% only about 0.2% irreversible strain could be identified. Following loading up to 4% about 0.6% residual strain accumulated. The relatively fast accumulation of residual strains indicates the activation of irreversible processes in

parallel to phase transformation. Thus, the formation of dislocations capable of pinning the evolving martensite phase boundaries can be expected [36–38]. Analysis of such elementary mechanisms is currently under investigation and will be reported in follow-up studies. Up to now, it is assumed that the martensitic phase boundaries are mechanically stabilized and the back transformation into the austenite is suppressed, as was already revealed for conventionally processed material [36–38].

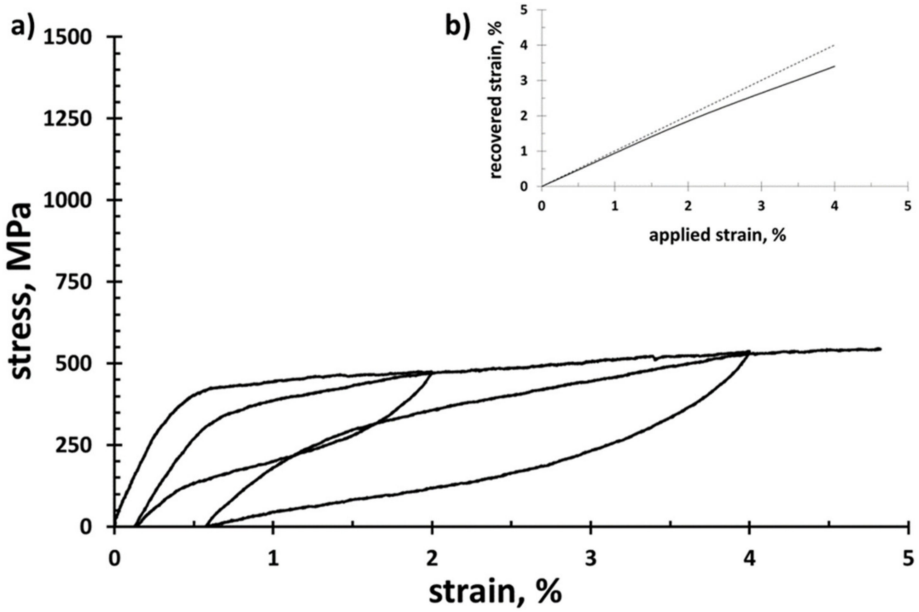

Figure 5. (**a**) Stress–strain response under tensile loading obtained from Fe-Mn-Al-Ni at RT after 5 HTC; (**b**) recovered strain plotted against the applied strain.

Figure 5b shows the applied strain plotted against the reversible strain. It can clearly be seen that the material shows a high reversibility upon loading in the very first superelastic cycle, i.e., loading to 2% strain. With further increase of the applied strain, the share of recovered strain decreases. This leads to the conclusion that the remaining grain constraints, imposed by the imperfect bamboo-like microstructure, dominated the evolution of residual strain. In this context, the loss of Mn is supposed to detrimentally affect the AGG process. Thus, the main challenge for further investigations will be the preservation of the chemical composition, as this can be seen as a key factor towards robust functional material properties in additively manufactured Fe-Mn-Al-Ni SMAs.

4. Conclusions

In the present work, laser powder bed fusion (L-PBF) processing of a Fe-Mn-Al-Ni shape memory alloy (SMA) at an elevated build platform temperature of 500 °C was conducted, followed by post-treatments, microstructure analysis, and tensile testing. The following conclusions could be drawn from the presented results:

1. L-PBF processing at 500 °C leads to crack-free Fe-Mn-Al-Ni bulk samples offering the possibility to fabricate individually designed, near-net-shaped parts by employing only one manufacturing step. This was not achieved so far due to the limited heating capabilities of most L-PBF systems available.
2. L-PBF processing leads to a noticeable change in chemical composition of the Fe-Mn-Al-Ni shape memory alloy. Mn is reduced by about 3 at. % upon L-PBF processing.
3. It is shown that a strong texture along the <001> direction primarily forms parallel to the build direction. However, the solidification microstructure is somehow affected by the geometry of the processed parts. In the as-built condition, an increase of the

diameter leads to a columnar grained microstructure and a strong texture in <001> direction.
4. Vicker's hardness measurements reveal a higher hardness in the as-built condition. This can likely be correlated to the formation of the β-Mn phase promoted by the elevated build platform temperature.
5. The application of a cyclic heat treatment promotes abnormal grain growth (AGG) in the L-PBF processed Fe-Mn-Al-Ni.
6. The microstructure established by the optimized heat treatment route is characterized by a good shape recovery ratio under tensile loading. However, elementary degradation mechanisms still limit the full potential of the L-PBF processed Fe-Mn-Al-Ni. A relatively fast accumulation of residual strains is seen promoted by prevailing grain constraints.

Author Contributions: F.C.E.: Visualization, Original Draft; F.B.: Conceptualization, Investigation, Review & Editing; T.G.: Conceptualization, Investigation, Review & Editing; M.V.: Conceptualization, Review & Editing; P.K.: Conceptualization, Visualization, Review & Editing; T.N.: Conceptualization, Review & Editing. All authors have read and agreed to the published version of the manuscript.

Funding: Financial support by DFG is acknowledged (Project No. 250216343).

Data Availability Statement: Data are available from the corresponding author on reasonable request.

Acknowledgments: T.G. thanks S. Pauly and U. Kühn for fruitful discussions, K. Schröder and N. Geißler for technical assistance, as well as A. Voß and H. Bußkamp for carrying out the chemical analysis of the powder and the additively manufactured material. In addition, D. Becker and U. Biscop are thanked for their outstanding support regarding the development of the high-temperature build envelope.

Conflicts of Interest: The authors declare no conflict of interest.

References

1. Mehrpouya, M.; Bidsorkhi, H.C. MEMS Applications of NiTi Based Shape Memory Alloys: A Review. *Micro Nanosyst.* **2017**, *8*, 79–91. [CrossRef]
2. Karaca, H.E.; Acar, E.; Tobe, H.; Saghaian, S.M. NiTiHf-based shape memory alloys. *Mater. Sci. Technol.* **2014**, *30*, 1530–1544. [CrossRef]
3. Enkovaara, J.; Ayuela, A.; Zayak, A.T.; Entel, P.; Nordström, L.; Dube, M.; Jalkanen, J.; Impola, J.; Nieminen, R.M. Magnetically driven shape memory alloys. *Mater. Sci. Eng. A* **2004**, *378*, 52–60. [CrossRef]
4. Karaca, H.E.; Karaman, I.; Basaran, B.; Ren, Y.; Chumlyakov, Y.I.; Maier, H.J. Magnetic Field-Induced Phase Transformation in NiMnCoIn Magnetic Shape-Memory Alloys-A New Actuation Mechanism with Large Work Output. *Adv. Funct. Mater.* **2009**, *19*, 983–998. [CrossRef]
5. Sato, A.; Chishima, E.; Soma, K.; Mori, T. Shape memory effect in $\gamma \rightleftarrows \epsilon$ transformation in Fe-30Mn-1Si alloy single crystals. *Acta Metall.* **1982**, *30*, 1177–1183. [CrossRef]
6. Tanaka, Y.; Himuro, Y.; Kainuma, R.; Sutou, Y.; Omori, T.; Ishida, K. Ferrous polycrystalline shape-memory alloy showing huge superelasticity. *Science* **2010**, *327*, 1488–1490. [CrossRef]
7. Omori, T.; Ando, K.; Okano, M.; Xu, X.; Tanaka, Y.; Ohnuma, I.; Kainuma, R.; Ishida, K. Superelastic effect in polycrystalline ferrous alloys. *Science* **2011**, *333*, 68–71. [CrossRef] [PubMed]
8. Sawaguchi, T.; Maruyama, T.; Otsuka, H.; Kushibe, A.; Inoue, Y.; Tsuzaki, K. Design Concept and Applications of Fe–Mn–Si-Based Alloys—From Shape-Memory to Seismic Response Control. *Mater. Trans.* **2016**, *57*, 283–293. [CrossRef]
9. Lee, D.; Omori, T.; Han, K.; Hayakawa, Y.; Kainuma, R. Effect of Thermomechanical Processing on Texture and Superelasticity in Fe–Ni-Co-Al–Ti-B Alloy. *Shap. Mem. Superelasticity* **2018**, *4*, 102–111. [CrossRef]
10. Lee, D.; Omori, T.; Kainuma, R. Ductility enhancement and superelasticity in Fe–Ni–Co–Al–Ti–B polycrystalline alloy. *J. Alloy. Compd.* **2014**, *617*, 120–123. [CrossRef]
11. Omori, T.; Okano, M.; Kainuma, R. Effect of grain size on superelasticity in Fe-Mn-Al-Ni shape memory alloy wire. *APL Mater.* **2013**, *1*, 32103. [CrossRef]
12. Ozcan, H.; Ma, J.; Wang, S.J.; Karaman, I.; Chumlyakov, Y.; Brown, J.; Noebe, R.D. Effects of cyclic heat treatment and aging on superelasticity in oligocrystalline Fe-Mn-Al-Ni shape memory alloy wires. *Scr. Mater.* **2017**, *134*, 66–70. [CrossRef]
13. Tseng, L.W.; Ma, J.; Wang, S.J.; Karaman, I.; Chumlyakov, Y.I. Effects of crystallographic orientation on the superelastic response of FeMnAlNi single crystals. *Scr. Mater.* **2016**, *116*, 147–151. [CrossRef]
14. Tseng, L.W.; Ma, J.; Wang, S.J.; Karaman, I.; Kaya, M.; Luo, Z.P.; Chumlyakov, Y.I. Superelastic response of a single crystalline FeMnAlNi shape memory alloy under tension and compression. *Acta Mater.* **2015**, *89*, 374–383. [CrossRef]

15. Vallejos, J.M.; Malarría, J.A. Growing Fe-Mn-Al-Ni single crystals by combining directional annealing and thermal cycling. *J. Mater. Process. Technol.* **2020**, *275*, 116317. [CrossRef]
16. Vollmer, M.; Arold, T.; Kriegel, M.J.; Klemm, V.; Degener, S.; Freudenberger, J.; Niendorf, T. Promoting abnormal grain growth in Fe-based shape memory alloys through compositional adjustments. *Nat. Commun.* **2019**, *10*, 2337. [CrossRef]
17. Vollmer, M.; Segel, C.; Krooß, P.; Günther, J.; Tseng, L.W.; Karaman, I.; Weidner, A.; Biermann, H.; Niendorf, T. On the effect of gamma phase formation on the pseudoelastic performance of polycrystalline Fe–Mn–Al–Ni shape memory alloys. *Scr. Mater.* **2015**, *108*, 23–26. [CrossRef]
18. Gibson, I.; Rosen, D.; Stucker, B. *Additive Manufacturing Technologies. 3D Printing, Rapid Prototyping and Direct Digital Manufacturing*; Springer: Berlin/Heidelberg, Germany, 2015.
19. Körner, C.; Helmer, H.; Bauereiß, A.; Singer, R.F. Tailoring the grain structure of IN718 during selective electron beam melting. In *MATEC Web of Conferences*; EDP Sciences: Les Ulis, France, 2014; Volume 14, p. 8001.
20. Thijs, L.; Kempen, K.; Kruth, J.-P.; van Humbeeck, J. Fine-structured aluminium products with controllable texture by selective laser melting of pre-alloyed AlSi10Mg powder. *Acta Mater.* **2013**, *61*, 1809–1819. [CrossRef]
21. Niendorf, T.; Brenne, F.; Schaper, M.; Riemer, A.; Leuders, S.; Reimche, W.; Schwarze, D.; Maier, H.J. Labelling additively manufactured parts by microstructural gradation—Advanced copy-proof design. *Rapid Prototyp. J.* **2016**, *22*, 630–635. [CrossRef]
22. Niendorf, T.; Leuders, S.; Riemer, A.; Richard, H.A.; Tröster, T.; Schwarze, D. Highly Anisotropic Steel Processed by Selective Laser Melting. *Met. Mater. Trans. B* **2013**, *44*, 794–796. [CrossRef]
23. Dadbakhsh, S.; Vrancken, B.; Kruth, J.-P.; Luyten, J.; van Humbeeck, J. Texture and anisotropy in selective laser melting of NiTi alloy. *Mater. Sci. Eng. A* **2016**, *650*, 225–232. [CrossRef]
24. Gustmann, T.; Neves, A.; Kühn, U.; Gargarella, P.; Kiminami, C.S.; Bolfarini, C.; Eckert, J.; Pauly, S. Influence of processing parameters on the fabrication of a Cu-Al-Ni-Mn shape-memory alloy by selective laser melting. *Addit. Manuf.* **2016**, *11*, 23–31. [CrossRef]
25. Haberland, C.; Elahinia, M.; Walker, J.M.; Meier, H.; Frenzel, J. On the development of high quality NiTi shape memory and pseudoelastic parts by additive manufacturing. *Smart Mater. Struct.* **2014**, *23*, 104002. [CrossRef]
26. Shiva, S.; Palani, I.A.; Mishra, S.K.; Paul, C.P.; Kukreja, L.M. Investigations on the influence of composition in the development of Ni–Ti shape memory alloy using laser based additive manufacturing. *Opt. Laser Technol.* **2015**, *69*, 44–51. [CrossRef]
27. Elahinia, M.; Shayesteh Moghaddam, N.; Taheri Andani, M.; Amerinatanzi, A.; Bimber, B.A.; Hamilton, R.F. Fabrication of NiTi through additive manufacturing: A review. *Prog. Mater. Sci.* **2016**, *83*, 630–663. [CrossRef]
28. Niendorf, T.; Brenne, F.; Krooß, P.; Vollmer, M.; Günther, J.; Schwarze, D.; Biermann, H. Microstructural Evolution and Functional Properties of Fe-Mn-Al-Ni Shape Memory Alloy Processed by Selective Laser Melting. *Met. Mat. Trans. A* **2016**, *47*, 2569–2573. [CrossRef]
29. Torrent, C.; Bauer, A.; Vollmer, M.; Niendorf, T. On the Challenges toward Realization of Functionally Graded Structures by Electron Beam Melting—Fe-Base Shape Memory Alloy and Stainless Steel. In *Structural Integrity of Additive Manufactured Materials and Parts*; Shamsaei, N., Seifi, M., Eds.; Selected technical papers STP 1631; ASTM International: West Conshohocken, PA, USA, 2020; pp. 20–33. [CrossRef]
30. Omori, T.; Iwaizako, H.; Kainuma, R. Abnormal grain growth induced by cyclic heat treatment in Fe-Mn-Al-Ni superelastic alloy. *Mater. Des.* **2016**, *101*, 263–269. [CrossRef]
31. Tseng, L.W.; Ma, J.; Hornbuckle, B.C.; Karaman, I.; Thompson, G.B.; Luo, Z.P.; Chumlyakov, Y.I. The effect of precipitates on the superelastic response of [100] oriented FeMnAlNi single crystals under compression. *Acta Mater.* **2015**, *97*, 234–244. [CrossRef]
32. Schwab, H.; Bönisch, M.; Giebeler, L.; Gustmann, T.; Eckert, J.; Kühn, U. Processing of Ti-5553 with improved mechanical properties via an in-situ heat treatment combining selective laser melting and substrate plate heating. *Mater. Des.* **2017**, *130*, 83–89. [CrossRef]
33. Frenck, J.-M.; Vollmer, M.; Mandel, M.; Krüger, L.; Niendorf, T. On the Influence of Microstructure on the Corrosion Behavior of Fe–Mn–Al–Ni Shape Memory Alloy in 5.0 wt% NaCl Solution. *Adv. Eng. Mater.* **2020**, 2000865. [CrossRef]
34. Huang, P.; Peng, H.; Wang, S.; Zhou, T.; Wen, Y. Relationship between martensitic reversibility and different nano-phases in a FeMnAlNi shape memory alloy. *Mater. Charact.* **2016**, *118*, 22–28. [CrossRef]
35. Tseng, L.W.; Ma, J.; Vollmer, M.; Krooß, P.; Niendorf, T.; Karaman, I. Effect of grain size on the superelastic response of a FeMnAlNi polycrystalline shape memory alloy. *Scr. Mater.* **2016**, *125*, 68–72. [CrossRef]
36. Gall, K.; Maier, H.J. Cyclic deformation mechanisms in precipitated NiTi shape memory alloys. *Acta Mater.* **2002**, *50*, 4643–4657. [CrossRef]
37. Vollmer, M.; Kriegel, M.J.; Krooß, P.; Martin, S.; Klemm, V.; Weidner, A.; Chumlyakov, Y.; Biermann, H.; Rafaja, D.; Niendorf, T. Cyclic Degradation Behavior of [001]-Oriented Fe–Mn–Al–Ni Single Crystals in Tension. *Shap. Mem. Superelasticity* **2017**, *3*, 335–346. [CrossRef]
38. Vollmer, M.; Krooß, P.; Kriegel, M.J.; Klemm, V.; Somsen, C.; Ozcan, H.; Karaman, I.; Weidner, A.; Rafaja, D.; Biermann, H.; et al. Cyclic degradation in bamboo-like Fe–Mn–Al–Ni shape memory alloys—The role of grain orientation. *Scr. Mater.* **2016**, *114*, 156–160. [CrossRef]